Heliyon 10 (2024) e36583

Contents lists available at ScienceDirect

Heliyon

journal homepage: www.cell.com/heliyon

Research article

The destruction of cytoplasmic skeleton leads to the change of nuclear structure and the looseness of lamin A submicroscopic network

Zhenyu Yang [a,b,1], Xianglong Liu [a,b,1], Xiaoliang Li [c,1], Maurizio Abbate [d], Han Rui [a,b], Miao Guan [e,**], Zhenglong Sun [a,b,f,*]

[a] State Key Laboratory of Primate Biomedical Research, Institute of Primate Translational Medicine, Kunming University of Science and Technology, Kunming, China
[b] Yunnan Key Laboratory of Primate Biomedical Research, Kunming, China
[c] ZEISS Research Microscopy Solutions, Shanghai, China
[d] Arivis AG, Rostock, Germany
[e] Faculty of Life Science and Technology, Kunming University of Science and Technology, Kunming, China
[f] Shenzhen Bay Laboratory, Shenzhen, China

ARTICLE INFO

Keywords:
Nucleus
Cytoplasmic skeleton
Lamin A
Super-resolution imaging
Chromosome

ABSTRACT

The interaction between lamin A and the cytoplasmic skeleton plays a key role in maintaining nuclear mechanical properties. However, the effect of destruction of the cytoplasmic skeleton on the 3D submicroscopic structure of lamin A has not been elucidated. In this study, we developed an image quantization algorithm to quantify changes in the submicroscopic structure of the intact lamin A 3D network within the nucleus. We used blebbistatin or nocodazole to disrupt the fibrillar structure of F-actin or tubulin, respectively, and then quantified changes in the lamin A super-resolution network structure, the morphological and mechanical properties of the nucleus and the spatial distribution of chromosomes. Ultimately, we found for the first time that disruption of the cytoplasmic skeleton changes the lamin A submicroscopic network and nuclear structural characteristics. In summary, this study contributes to understanding the trans-nuclear membrane interaction characteristics of lamin A and the cytoplasmic skeleton.

1. Introduction

Various basic physiological functions of the cell, such as organelle transport, cell division and migration, are mainly supported by the cytoskeleton, which is composed of three filamentous proteins: microfilaments, microtubules, and intermediate filaments [1]. A variety of cytoskeletal proteins cross-link and interact with each other to provide a whole cytoskeletal network, which contributes to the morphogenesis and signal transduction of cells [2,3]. Lamins are type V intermediate filaments found in the nucleus of mammalian cells and consist of lamin A, lamin B1 and lamin B2. Mature lamins interact through the central α helix domain to form a globular

* Corresponding author. State Key Laboratory of Primate Biomedical Research, Institute of Primate Translational Medicine, Kunming University of Science and Technology, Kunming, China.
** Corresponding author.
E-mail addresses: mguan2021@hotmail.com (M. Guan), jssuqian2001@hotmail.com (Z. Sun).
[1] These authors have contributed equally to this work and share the first authorship.

https://doi.org/10.1016/j.heliyon.2024.e36583
Received 1 April 2024; Received in revised form 14 August 2024; Accepted 19 August 2024
Available online 7 September 2024

network structure on the nucleoplasmic side of the inner nuclear membrane (INM) [4]. The lamins network regulates the mechanics of the nucleus and the transcriptional activity of chromatin [5].

The lamin A protein, encoded by the *LMNA* gene, plays a more significant role than lamin B in regulating the stiffness and elasticity of the nucleus [6,7]. The fibrous lamin A protein is anchored to the nucleoplasmic side of INM via associations with the N-terminal domain of the SUN protein [8,9]. Lamin A physically couples with the cytoplasmic skeleton through interaction between SUN and nesprins in the nuclear membrane [10–12]. The cytoplasmic skeleton interacts with lamin A network to form an overall mechanical structure that is involved in regulating cell nuclear mechanical signals and morphological characteristics [13,14]. When lamin A is knocked out, the amount of F-actin in the cell center is reduced, and the nucleus becomes larger, rounder and thicker [15,16]. The

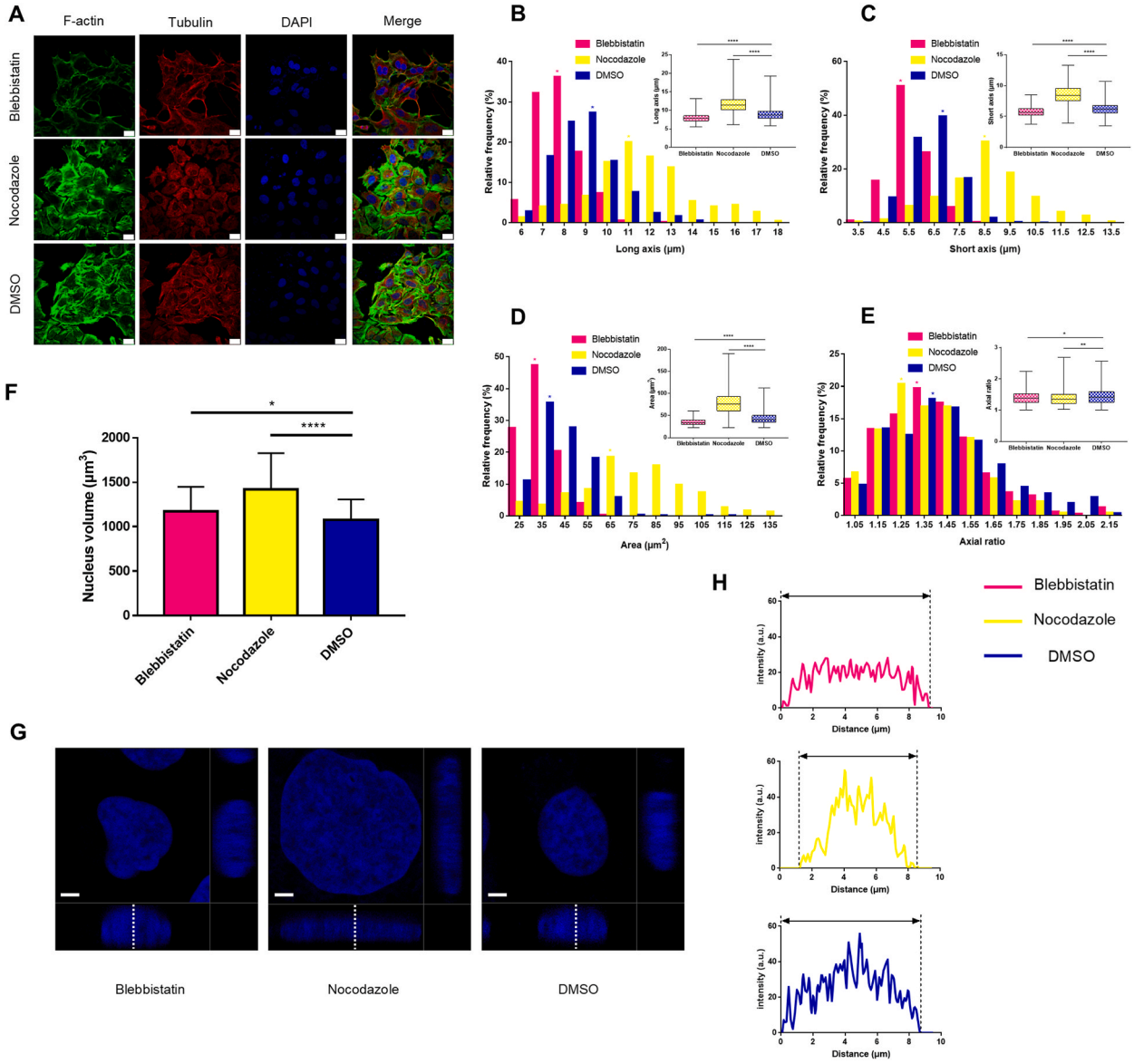

Fig. 1. The morphological characteristics of nuclei in U2OS cells were changed by blebbistatin or nocodazole. (A) The filamentary structure of F-actin or tubulin was destroyed with blebbistatin or nocodazole, as based on confocal microscopy. Scale bar, 25 μm. (B–E) Quantitative analysis of changes in nuclear morphological characteristics at the X-Y projection plane. The long axis length (B), short axis length (C) and nuclear area (D) decreased after blebbistatin treatment and increased after nocodazole treatment. The ratio of the long axis to short axis (E) decreased after treatment with blebbistatin or nocodazole. The significant difference among the groups, *$p < 0.05$, **$p < 0.01$, ****$p < 0.0001$. (F) Quantitative analysis of the changes in nuclear volume after blebbistatin or nocodazole treatment. The significant difference among the groups, *$p < 0.05$, ****$p < 0.0001$. (G) Confocal image of U2OS nuclei with DAPI in the X-Y, X-Zand Y-Z planes. The height of the nucleus was measured in the X-Z plane. Scale bar 5 μm. (H) The fluorescence distribution on the white dotted line in G. The height of the nucleus increased after blebbistatin treatment and decreased after nocodazole treatment.

deficiency of lamin A also leads to defective ciliogenesis [17]. Moreover, mutations in the *LMNA* gene result in disarray of microtubule network and shorter microtubule fibers [18]. Although it has been confirmed that changes in the lamin A network affect the structure of the cytoplasmic skeleton, the effect of breaking the cytoplasmic skeleton on the lamin A submicroscopic network is still unknown.

The development of super-resolution microscopy made it possible to analyze the submicroscopic structure of the lamin A network by optical imaging [19–21]. The lamin A submicroscopic network can be clearly observed by super-resolution microscopy, yet

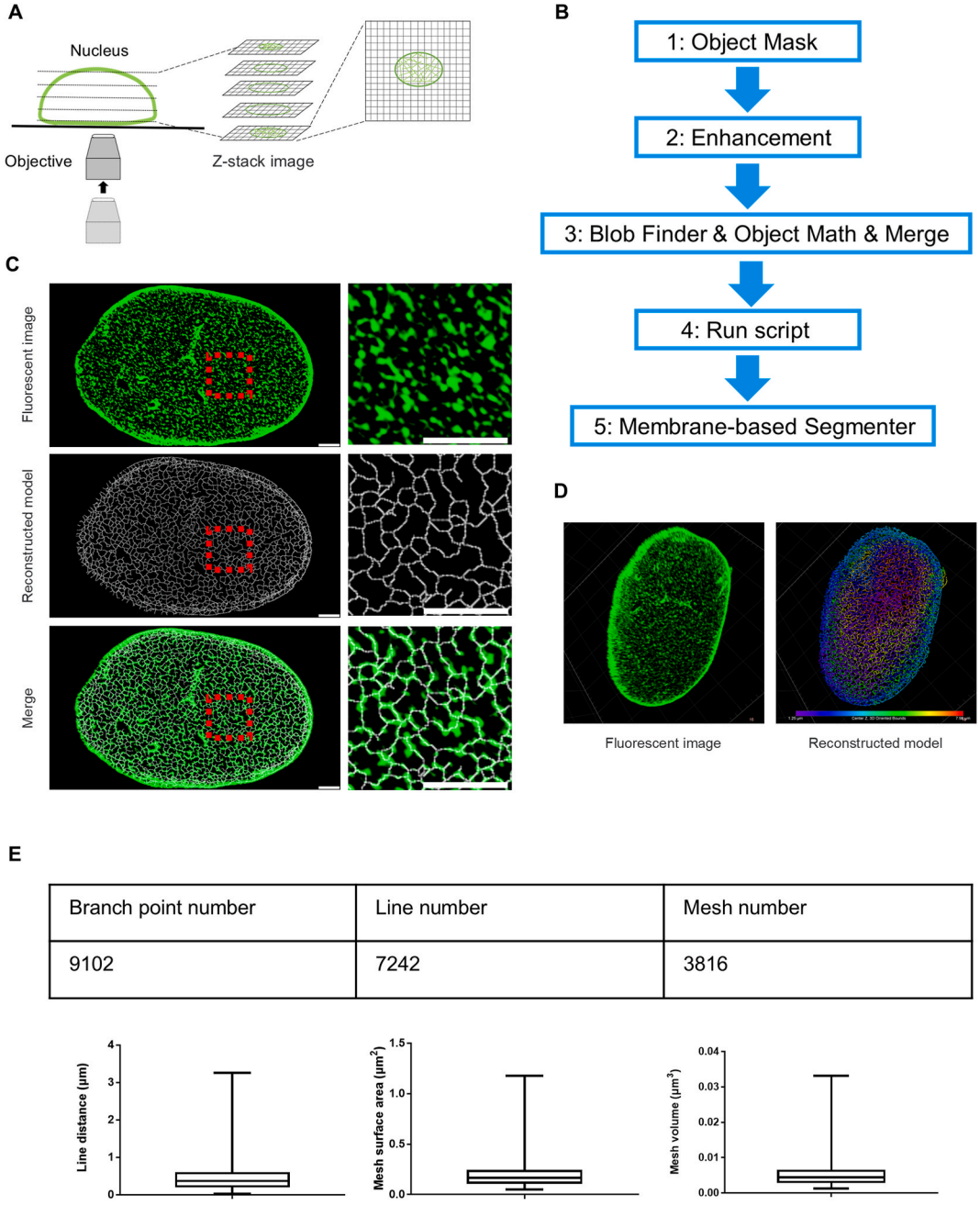

Branch point number	Line number	Mesh number
9102	7242	3816

Fig. 2. A quantitative analysis method for lamin A 3D superresolution fluorescence imaging. (A) Schematic diagram of 3D super-resolution imaging of the whole lamin A network by Lattice SIM in the Z-stack. (B) Process for the image quantization algorithm of lamin A fluorescence images. (C) The fluorescence image, reconstructed model and merged image of the lamin A submicroscopic network on the X-Y plane. The left image shows the maximum intensity projection of the lamin A network from 11 Z-stacks near the bottom of the nucleus. The right image is the enlarged diagram of the dotted box of the left image. Scale bar 2 μm. (D) 3D fluorescence image and reconstructed model of the whole lamin A network in 50 Z-stacks. (E) Submicroscopic structural features obtained from the reconstructed lamin A network model. The submicroscopic structural features include the branch point number, line number, mesh number, line distance, mesh surface area and mesh volume of lamin A. Data are represented as mean ± SD.

quantitative analysis of the lamin A network remains a great challenge. The 3D network of lamin A plays an essential role in registering the mechanical properties of the nucleus, and quantitative analysis of the lamin A 3D submicroscopic network will help in understanding the regulatory characteristics of the nuclear skeleton on nuclear mechanical properties. However, most quantitative studies involving the lamin A submicroscopic network only perform analysis of lamin A networks projected on the X-Y plane, whereas few studies have focused on analysis of the complete 3D network of lamin A [19,21,22]. Recently, a method for lamin B1 3D super-resolution image analysis was proposed [23]. The research used stochastic optical reconstruction microscopy (STROM) together with multiplane acquisition to image the whole lamin B1 network of COS-7 and T cells in 3D. Although the study quantified the overall characteristics of the 3D lamin B1 network, the distribution and structural characteristics of the submicroscopic meshes and protein fibers of lamin in the overall 3D structure were not quantified.

In this study, we disrupted the fibrous structure of F-actin or tubulin by blebbistatin or nocodazole, respectively, and then quantified the morphological and mechanical properties of the nucleus, the super-resolved structure of the lamin A network and the spatial distribution of chromatin. To explore the effect of the cytoplasmic skeleton on the lamin A submicroscopic network, we used lattice structured illumination microscopy (Lattice SIM) to perform Z-stack imaging of the whole lamin A network after F-actin or tubulin were destroyed. For the super-resolution fluorescence image, we developed an image quantization algorithm based on fluorescence signal voxel analysis to quantify changes in the submicroscopic structure of the whole lamin A network. Our research findings indicate the effects of the cytoplasmic skeleton on the nuclear structure and lamin A submicroscopic network and promote investigation of the interaction characteristics between lamin A and the cytoplasmic skeleton.

2. Results

2.1. Disruption of the cytoplasmic skeleton changes the nuclear morphology

The cytoskeleton plays a key role in cellular mechanical stability. In this study, blebbistatin and nocodazole were used to understand the effect of cytoplasmic skeleton destruction on nuclear morphology. Blebbistatin is a specific inhibitor of nonmuscle myosin II and prevents cross-linking of rigid actomyosin by binding to the myosin-ADP-Pi complex [24,25]. Nocodazole interferes with the structure of microtubules in mammalian cells and results in their disassembly [26]. For optimal disruption of the cytoplasmic skeleton without excessively affecting the cellular state, 25 μM blebbistatin or 2 μM nocodazole were used to disrupt F-actin or tubulin, respectively [27–29]. We found that the fiber structures of F-actin or tubulin were disassembled 8 h after treatment with drug [30–33] (Fig. 1A). When cytoplasmic skeleton was destroyed, nucleus morphology was changing, and more binucleated cells appeared after blebbistatin treatment (Fig. 1A and Fig. S1). In the X-Y plane, the long axis, short axis and area of the DMSO group were 8.9 μm, 6.2 μm and 42.9 μm^2, respectively. The long axis, short axis and area of the nucleus decreased to 7.9 μm, 5.7 μm and 35.3 μm^2, respectively, when the cells were treated with blebbistatin; the long axis, short axis and area of the nucleus increased to 11.7 μm, 8.5 μm and 78.5 μm^2, respectively, with nocodazole treatment (Fig. 1B–D). After treatment with blebbistatin or nocodazole, the long-to-short axis ratio of the nucleus decreased significantly from 1.45 to 1.40 or 1.39. This indicates that when the cytoplasmic skeleton was destroyed, the projection of the nucleus in the X-Y plane became more rounded (Fig. 1E). The volume of the nucleus also increased as the cells were treated with blebbistatin or nocodazole (Fig. 1F). In the X-Z plane, the height of the nucleus increased when cells were treated with blebbistatin, but it decreased with nocodazole treatment (Fig. 1G and H). Thus, disruption of the cytoplasmic skeleton significantly affects the morphological features of the nucleus. Lamin A plays a more essential role in nuclear mechanical properties than lamin B [7,34], and the morphology of the nucleus is maintained by the interaction of lamin A with F-actin and tubulin [35,36]. Therefore, after destroyed the cytoplasmic skeleton, the changes in nuclear morphological characteristics suggested that the cytoplasmic skeleton may also affect the characteristics of the lamin A network.

2.2. Quantitative analysis of lamin A submicroscopic network

We further investigated how cytoplasmic skeleton disruption affects the fine network of lamin A. For a convenient and accurate elucidation of the lamin A network, Lattice SIM was used to image the whole 3D super-resolution network of it with 110 nm X-Y resolution and 200 nm Z resolution (Fig. 2A and Movie S1). 50 Z-stacks covering the whole nuclei with a step size of 0.1 μm were taken for lamin A. To characterize the lamin A network quantitatively, a voxel extraction-dependent algorithm was designed and applied to analyze its properties (Fig. 2B and Fig. S2). The network model of lamin A were reconstructed by extracting fluorescence signal data in 3D (Fig. 2C and D and Movie S2). Examination of the microstructure features of lamin A also revealed the number, surface area and volume of the lamin A 3D mesh (Fig. 2E); the line distance, branch point number and line number of lamin A fibers were also obtained (Fig. 2E). With the above analysis process, the network of lamin A was accurately quantified.

Supplementary video related to this article can be found at doi:10.1016/j.heliyon.2024.e36583

2.3. Disruption of the cytoplasmic skeleton reduces the denseness of the lamin A submicroscopic network

To investigate the effect of cytoplasmic skeleton disruption on the lamin A structure, the lamin A 3D network after blebbistatin or nocodazole treatment was imaged by Lattice SIM (Fig. 3A and Movie 3-5). The lamin A 3D submicroscopic network model was obtained through reconstruction based on the image quantization algorithm which using the fluorescence image of lamin A (Fig. 3A and B and Movies 6-8). Through holistic analysis of the lamin A network model, the surface area of the whole network in the DMSO group was 968.47 μm^2. The surface area of the whole lamin A network was 901.77 μm^2 due to treatment with blebbistatin and 1166.68 μm^2

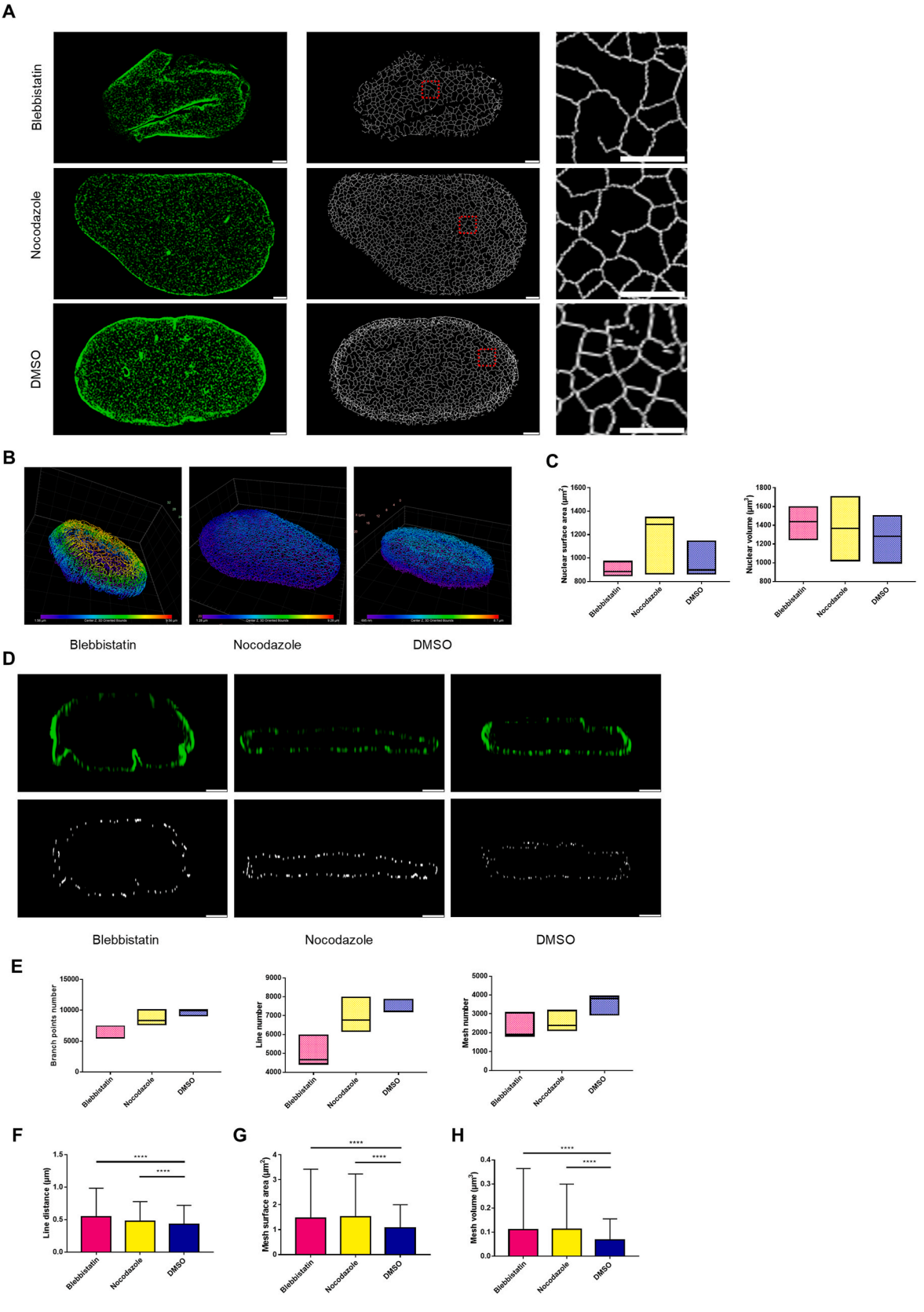

(caption on next page)

Fig. 3. Changes in the 3D submicroscopic structure of lamin A after blebbistatin or nocodazole treatment. (A) The maximum intensity projection of the fluorescence images (left) and reconstructed model (middle) of lamin A from 11 Z-stacks near the bottom of the nucleus after treatment with blebbistatin or nocodazole. The right image is the enlarged diagram of the dotted box of the middle image. Scale bars are 2 μm in the left and middle images and 1 μm in the right image. (B) The whole 3D structure of the reconstructed model of the lamin A network after blebbistatin or nocodazole treatment. (C) The overall surface area and volume of the nucleus after treatment with blebbistatin or nocodazole. (D) A screenshot of fluorescence images (top) and reconstructed model (bottom) of the lamin A network in the X-Z plane. Scale bar 2 μm. (E) Quantitative comparison analysis of the branch point number, line number and mesh number of the lamin A submicroscopic network. (F–H) Quantitative comparison analysis of the line distance (F), mesh surface area (G) and mesh volume (H) of the lamin A submicroscopic network. After blebbistatin or nocodazole treatment, the line distance, mesh surface area and mesh volume of the lamin A network increased significantly. Data are represented as mean ± SD. The significant difference among the groups, ****$p < 0.0001$.

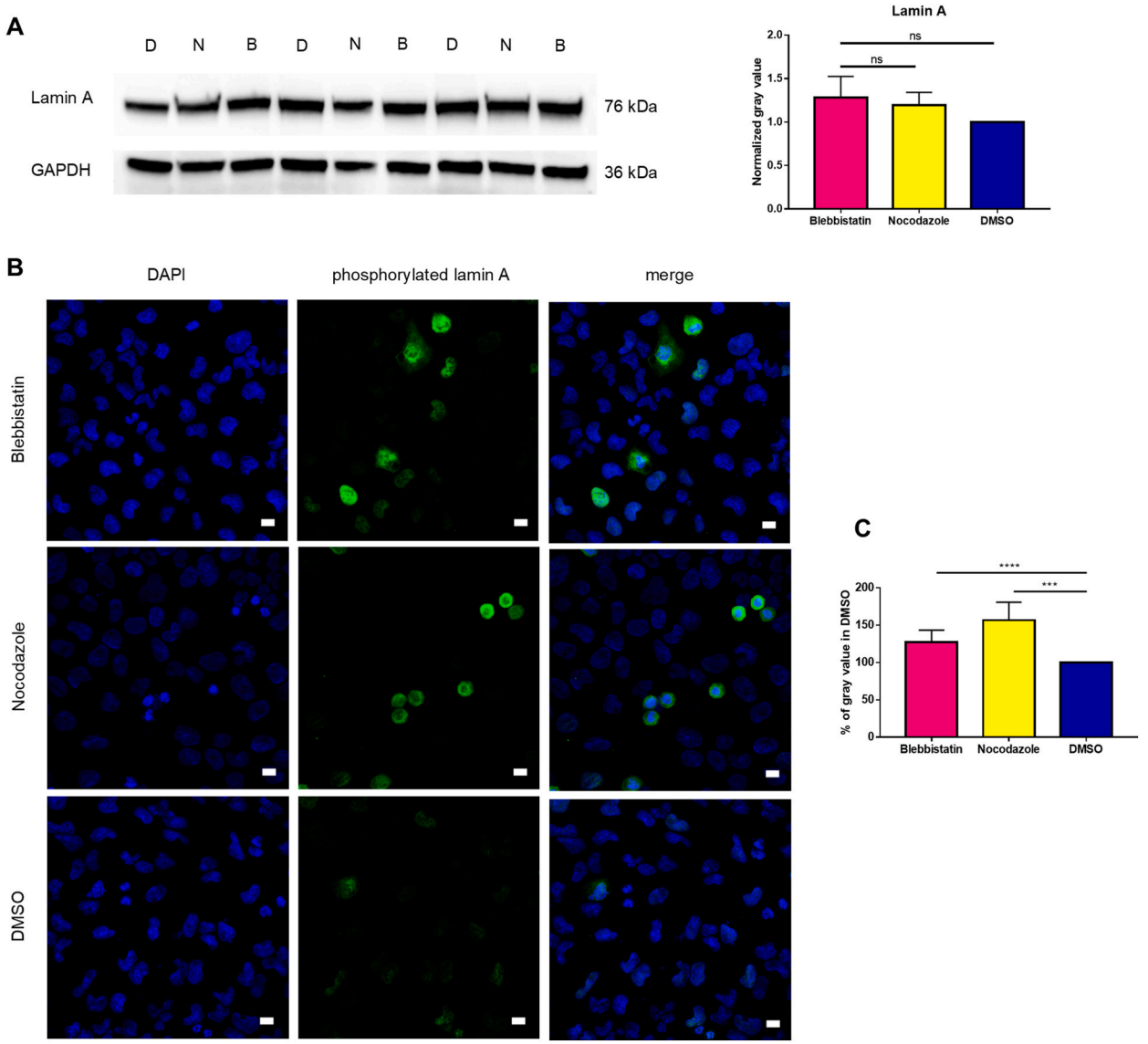

Fig. 4. Effect of blebbistatin or nocodazole on lamin A and phosphorylated lamin A contents in cells. (A) Protein expression of lamin A in cells after blebbistatin or nocodazole treatment was detected by western blotting. After blebbistatin or nocodazole treatment, level of lamin A was unchanged. The left image shows the protein bands in the Western blot. The right image shows the gray value statistics of the protein bands. D: DMSO, B: Blebbistatin, N: Nocodazole. Data are represented as mean ± SD. The significant difference among the groups, ns, not significant. (B) Representative fluorescence maximum intensity projection images of phosphorylated lamin A and DAPI. Scale bar: 10 μm. (C) Histogram of the percentage of fluorescence gray value of phosphorylated lamin A images (B) after treated with blebbistatin or nocodazole compared with the DMSO group. After blebbistatin or nocodazole treatment, the content of phosphorylated lamin A in cells increased. Data are represented as mean ± SD. The significant difference among the groups, ***$p < 0.001$, ****$p < 0.0001$.

due to treatment with nocodazole. The volume of the nucleus surrounded by lamin A was 1259.94 μm^3 in the DMSO group, 1426.18 μm^3 in the blebbistatin treatment group and 1364.30 μm^3 in the nocodazole treatment group (Fig. 3C). In the X-Z plane, the height of the lamin A network showed an increasing or decreasing trend with blebbistatin or nocodazole treatment, which is similar to the DAPI images (Fig. 1G and H and 3D). There were some internal lamin A foci in the nucleus called the nucleoplasmic reticulum, which promote the nuclear export of rRNA and regulate chromatin transcriptional activity [37] (Fig. 3A). However, when the F-actin was destroyed, the surface of the lamin A network appeared a narrow invagination with a morphology different from the nucleoplasmic reticulum, which represented a slack state of the nuclear envelope [38] (Fig. 3A and D). The above results suggest that damage to the cytoplasmic skeleton leads to changes in the morphology of the overall lamin A network.

Supplementary video related to this article can be found at doi:10.1016/j.heliyon.2024.e36583

To further resolve the effects of disruption of the cytoplasmic skeleton on the submicrostructure of the lamin A network, detailed information on the lamin A fibers and meshes were extracted from the lamin A-reconstructed model. Using submicrostructural analysis of lamin A fibers, we found that the number of branch points was reduced from 9688 to 6418 or 8698 after the treatment of blebbistatin or nocodazole, respectively (Fig. 3E) and the number of lamin A fibers was reduced from 7433 to 5020 or 6967, respectively (Fig. 3E). However, the lamin A fiber length increased significantly from 0.43 μm to 0.54 μm or 0.47 μm due to blebbistatin or nocodazole treatment, respectively (Fig. 3F). For analysis of lamin A submicroscopic 3D meshes, the number of meshes decreased from 3567 to 2267 or 2564 after blebbistatin or nocodazole treatment (Fig. 3E). The surface area of the meshes increased significantly from 1.07 μm^2 to 1.47 μm^2 or 1.52 μm^2, respectively, and the volume of the meshes from 0.070 μm^3 to 0.110 μm^3 or 0.112 μm^3, respectively, with blebbistatin or nocodazole (Fig. 3G and H). Integrating the above data, damaging the cytoplasmic skeleton changes the structural characteristics of the overall lamin A network and induces a relaxed lamin A submicroscopic network structure, which in turn potentially alters the morphological characteristics of the nucleus.

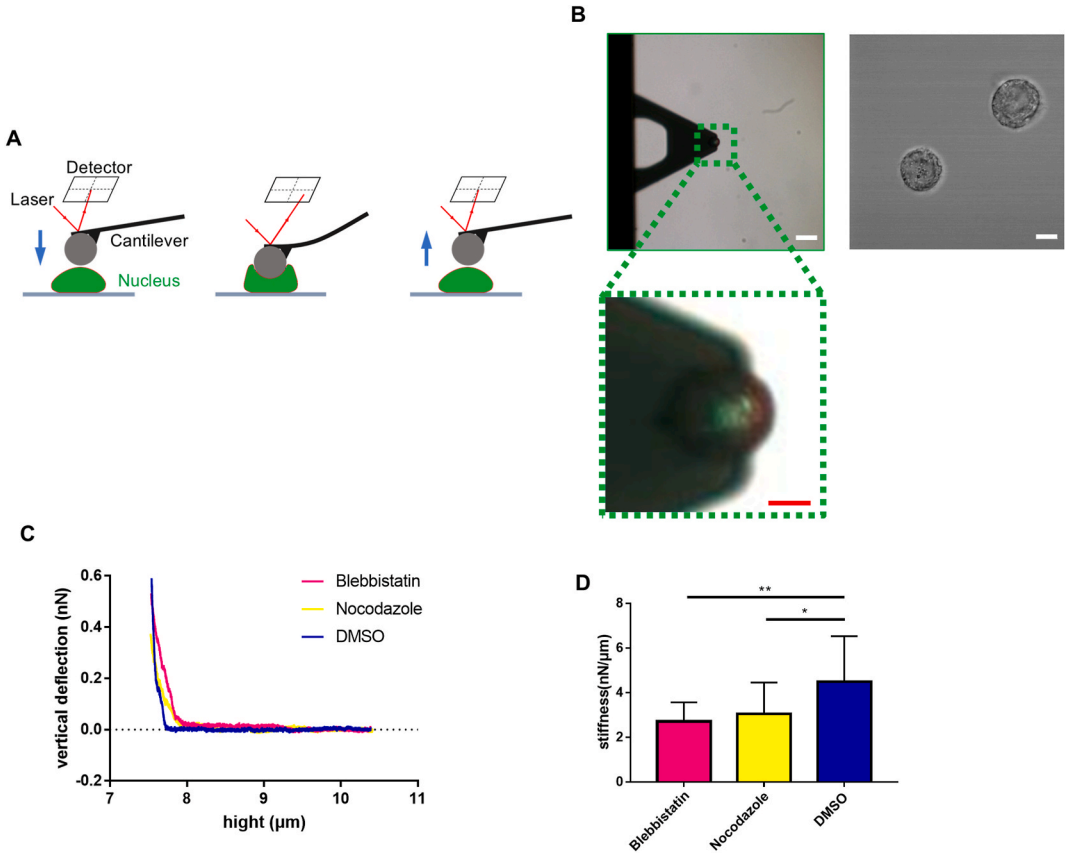

Fig. 5. The effect of blebbistatin or nocodazole on nuclear stiffness. (A) Schematic diagram of the AFM to measure nuclear stiffness. The cantilever approaches the nucleus surface with a predefined contact force causing nucleus deformation, and the counterforce on the bending cantilever was measured as the deflection of a laser beam reflected from the cantilever's apex onto a detector. (B) Brightfield microscopy image of bead-functionalized ScanAsyst-Fluid cantilever (left top) and the extracted nucleus (right). Magnified views of the boxed regions in the left image reveal that the polystyrene bead with a diameter of 9 μm was functionalized to the tip of the cantilever in the high light intensity image (left bottom). Scale bar: 5 μm. (C) Representative force-penetration curves of each group with a standard contact force using the bead-functionalized ScanAsyst-Fluid cantilever. (D) Histogram of nuclear stiffness. The nuclear stiffness of each group was derived from the extracted nucleus, and 5 repetitions were measured per nucleus. After blebbistatin or nocodazole treatment, nuclear stiffness decreased significantly. Data are represented as mean ± SD. The significant difference among the groups, *$p < 0.05$, **$p < 0.01$.

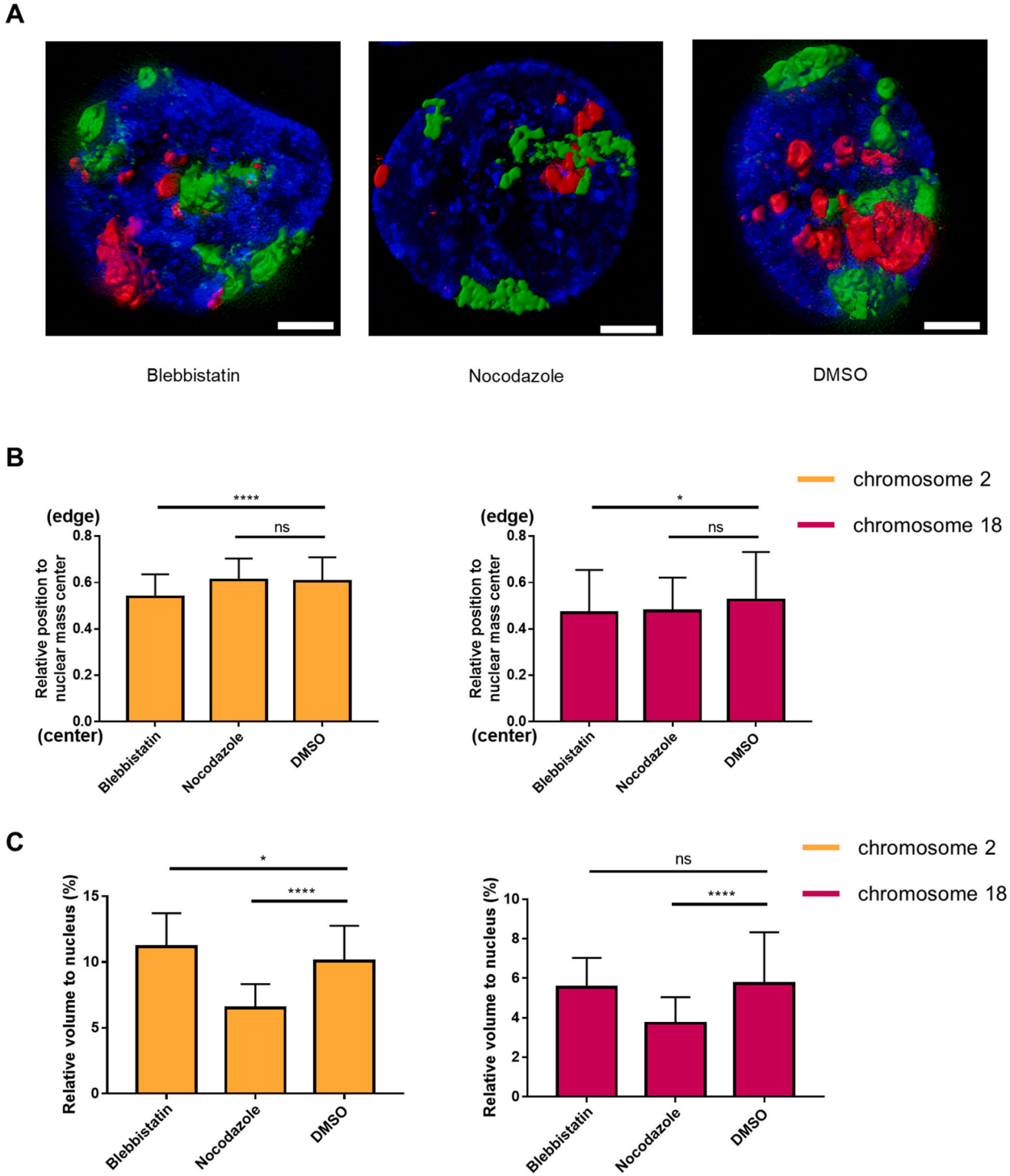

Fig. 6. Effect of destruction of the cytoplasmic skeleton on the spatial distribution of chromosomes in the nucleus. (A) Representative images of the spatial distribution of chromosome 2 (green) and chromosome 18 (red) within the nucleus of cells with blebbistatin, nocodazole or DMSO treatment. Scale bar: 2 μm. (B) Histogram of the relative position of chromosomes 2 and 18 within the nucleus. After blebbistatin treatment, the position of chromosomes 2 and 18 in the nucleus was closer to the center. Data are represented as mean ± SD. The significant difference among the groups, *p < 0.05, ****p < 0.0001, ns, not significant. (C) Histogram of the relative volume of chromosomes 2 and 18 within the nucleus. After blebbistatin treatment, the volume of chromosome 2 relative to the nucleus increased. After nocodazole treatment, the volume of chromosomes 2 and 18 relative to the nucleus decreased. Data are represented as mean ± SD. The significant difference among the groups, *p < 0.05, ****p < 0.0001, ns, not significant.

2.4. Disruption of the cytoplasmic skeleton increase the content of phosphorylated lamin A

The lamin A network plays a crucial role in maintaining of morphological characteristics in the nucleus [6,35]. The changes in lamin A content in cells may lead to the change of the lamin A network [4,16]. To investigate the effect of cytoskeletal disruption on lamin A content, expression of lamin A was examined. Western blot analysis showed no significant variation in lamin A expression after cells were treated with blebbistatin or nocodazole (Fig. 4A). Therefore, destruction of the cytoplasmic skeleton does not change the submicroscopic network of lamin A by changing its expression.

Phosphorylation of lamin A at Ser 22 promotes depolymerization of the lamin A 3D network in the nucleus [39,40]. To investigate whether blebbistatin and nocodazole influence the lamin A network through phosphorylation of lamin A, expression of phosphorylated lamin A was examined by immunofluorescence assay (Fig. 4B). In the fluorescence images, more diffuse phosphorylated lamin A rather than fibrous's appeared in cells after blebbistatin or nocodazole treatment. Mean fluorescence gray value analysis confirmed significantly increased content of phosphorylated lamin A with blebbistatin or nocodazole (Fig. 4C). The mean fluorescence gray value of phosphorylated lamin A was 127.5 % in blebbistatin-treated cells and 156.7 % in nocodazole-treated cells compared to the DMSO group. Collectively, these data suggest that the cytoplasmic skeleton potentially affects the lamin A submicroscopic network through the phosphorylation of lamin A.

2.5. Disruption of the cytoplasmic skeleton reduce the nuclear stiffness

The mechanical properties of the nucleus are primarily maintained by lamin A [41]. Destruction of the cytoplasmic skeleton leads

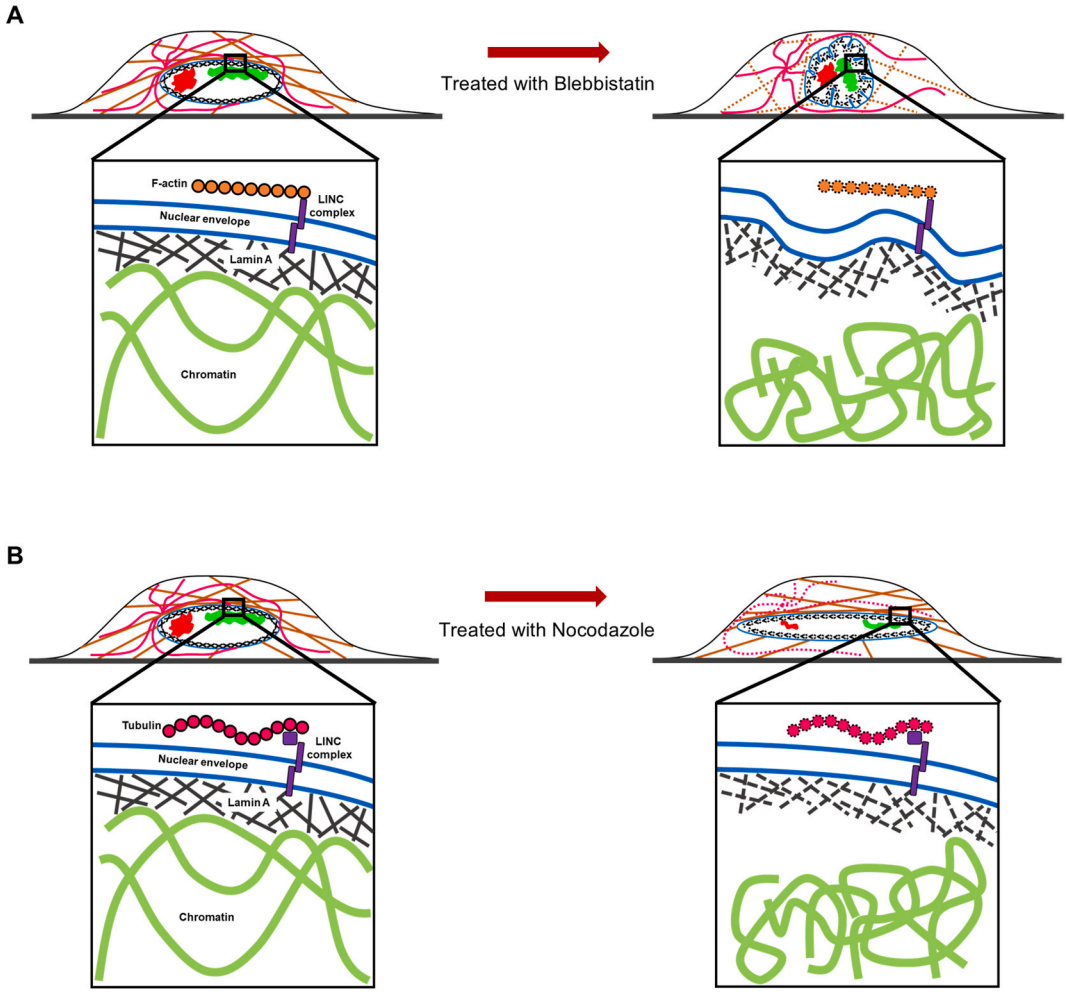

Fig. 7. Schematic diagram of the change in cytoskeletal and nuclear morphology after blebbistatin or nocodazole treatment. (A) After blebbistatin treatment, the fiber structure of F-actin was destroyed. The height of the nucleus was increased, and folds appeared on the nuclear membrane. The lamin A network and the spatial distribution of chromosomes were changed. (B) After nocodazole treatment, the fiber structure of tubulin was destroyed. The height of the nucleus was decreased. The lamin A network and the chromosome spatial position were changed.

to changes in the lamin A network. Therefore, the stiffness of the nucleus may change due to destruction of the cytoplasmic skeleton. The stiffness of the nucleus treated with blebbistatin or nocodazole was measured by atomic force microscopy (AFM). The force-penetration curves of the nucleus were derived by using a cantilever adhered with 9 μm polystyrene spheres to measure the stiffness of the extracted nucleus (Fig. 5A and B). The slope of the force-penetration curves was significantly less than the DMSO group when cells were treated with blebbistatin or nocodazole (Fig. 5C). By analyzing the force-penetration curves, we found that the nucleus stiffness decreased from 4.49 nN/μm to 2.71 nN/μm or 3.03 nN/μm after blebbistatin or nocodazole treatment, respectively (Fig. 5D). These results indicate that disruption of the cytoplasmic skeleton affects the mechanical characteristics of the nucleus.

2.6. Disruption of the cytoplasmic skeleton changes the spatial distribution of chromosome

Lamin A binds to the parts of chromatin and is involved in regulating the transcriptional activity of chromatin [42,43]. To investigate the effect of cytoplasmic skeleton disruption on chromosome distribution, chromosome painting was used to examine the spatial location and the relative volume of chromosomes 2 and 18. The gene-poor chromosome 18 contains less lamina-associated domain (LADs) than chromosome 2, therefore chromosome 2 interacts more with lamin A and is located in the peripheral region of the nucleus, while chromosome 18 is located in the interior region of the nucleus compared with chromosome 2 [44]. Following DNA fluorescent probe hybridization, chromosomes 2 and 18 were imaged by Lattice SIM in the Z-stacks. The volume and centroid position of the chromosome and nucleus can be directly obtained by surface rendering the 3D images on IMARIS software (Fig. 6A). The distance between chromosomes and the nucleus center was normalized by the cube root of the nucleus volume. After blebbistatin treatment, relative distances between chromosomes 2 and 18 and the center of the nucleus decreased from 0.60 to 0.53 to 0.54 and 0.47, respectively (Fig. 6B). This indicates that the destruction of F-actin causes the spatial position of chromosomes 2 and 18 to be closer to the central region in the nucleus, which may affect the transcriptional activity of the chromosome [45]. The volume of the 3D fluorescent signal of the probe is intimately related to the looseness and transcriptional activity of chromatin [45]. By analyzing chromosome volume relative to the nucleus, we found that the relative volume of chromosomes 2 and 18 decreased from 10.06 % to 5.73 %–6.50 % and 3.72 %, respectively, after nocodazole treatment. The relative volume of chromosome 2 increased to 11.18 % after blebbistatin treatment (Fig. 6C). This indicates that destruction of tubulin reduces the volume of chromosomes 2 and 18 as well as renders them more condensed. The destruction of F-actin will lead to an increased chromosome 2 vol and looser agglutination. These results suggest that disruption of the cytoplasmic skeleton affects the spatial distribution of chromosome in the nucleus.

3. Discussion

The whole morphological structure of cells is regulated by both cytoplasmic and nuclear skeletons. The cytoplasmic skeleton is connected to the nuclear skeleton lamin A protein via the linker of nucleoskeleton and cytoskeleton (LINC) complexes, which include SUN, Emerin, Luma, and nesprins [8,46]. Numerous studies have shown that the damage to the lamin A network leads to an abnormal cytoplasmic skeleton [16–18]. In contrast, few studies have quantified the specific effects on nuclear structure and the lamin A submicroscopic network due to various cytoplasmic skeletons. To investigate this, we used blebbistatin or nocodazole to disrupt the fibrous structure of microfilaments or microtubules, respectively [24,26]. Following disruption of the cytoplasmic skeleton, the nuclear morphology and the submicroscopic network of lamin A fibers were altered, as were nuclear stiffness and the chromosome spatial distribution. In general, destruction of the cytoplasmic skeleton causes the lamin A network to be much looser and changes the nuclear stiffness and spatial distribution of chromosomes (Fig. 7).

The mesh diameters and fiber lengths of lamin A in the nucleus were less than 200 nm, preventing accurate observation and quantitative analysis with conventional light microscopy [22]. To avoid the complex sample preparation and image localization errors associated with stimulated emission depletion microscopy (STED) and stochastic optical reconstruction microscopy (STROM), we used Lattice SIM to image the complete lamin A network in a fast Z-stack at 110 nm X-Y resolution. Previous studies have quantitatively analyzed the 2D network characteristics of lamin A in the X-Y plane [19,21,22], but quantitative description of the overall 3D network in lamins remains challenging. The study of Kittisopikul et al. demonstrated a method to construct 3D orientation space of lamins by augmenting a 2D image, which optimized the disadvantage of the lack of 3D spatial information when quantifying lamins in 2D [47]. A fluorescent point density-based convex hull fitting was used to analyze the overall structural characteristics of the lamin B1 3D network [23]. The lamin B1 surface was used as the nucleus boundary at the convex hull fitting for determining the surface area and volume of the nucleus. Based on above studies, we developed a super-resolution image quantization algorithm based on voxel extraction of fluorescent signals. The algorithm can not only determine the surface area and volume of the nucleus bounded by the whole lamin A network, but also identify the line distance and branch point number of lamin A fibers according to the distribution trend of the fluorescence signals. Indeed, we obtained detailed information about the mesh volume, mesh surface area and mesh number of the lamin A submicroscopic 3D network. The algorithm provides abundant and more detailed information than 2D lamins network resolution, which is performed only in the X-Y projection plane [22]. Our method first realized quantitative analysis of the characteristics of the complete lamin A network in 3D and will promote research on the submicroscopic structure of lamins.

Numerous cytoskeletons jointly regulate the morphology of the nucleus [1,13]. Abnormally enhanced assembly of tubulin or disruption of actin causes production of multilobed nuclei or changes in the morphology of nuclei [48,49]. This indicates that changes in the cytoplasmic skeleton can affect nuclear morphology. In 2D cultured cells, the actin cap generates an extrusion force in the axial direction of the nucleus and flattens its surface [16,38]. Similar to our study, the altered structure of the actin fibrils results in uneven mechanical forces and numerous folds on the nuclear surface of 2D cultured cells [38]. Tubulin fibers are randomly distributed in the cytoplasm and can also produce extrusion forces on the nucleus [50,51]. In our study, the height of the nucleus increased and the

projected area of the nucleus in the X-Y plane decreased with disruption of F-actin fibrils. The height and projected area of the nucleus in the X-Y plane also decreased and increased, respectively, with disruption of tubulin fibrils. Thus, our research suggests that F-actin and tubulin fibers may act mechanically on the cytoplasmic side of the nucleus by extrusion forces in various directions in 2D cultured interphase cells. Overall, the various mechanical forces of F-actin, tubulin and lamin A fibers balance each other and collectively maintain the morphological structure of the nucleus.

An intact cytoskeleton is the basis for normal cell morphology. Alterations in the structure of one cytoskeleton affect the structure of other cytoskeleton regularly. Many studies have confirmed that disruption of the LINC complex structure leads to a change in the organization of the cytoplasmic skeletal network and uncoupling of the cytoplasmic skeleton from the nucleus [52,53]. Additionally, disassembly of the cytoplasmic skeleton releases the tension of the LINC complex on the surface of the nucleus [54,55]. This suggests a tight mechanical force linking the cytoplasmic skeleton to the LINC complex and that the mechanical force will be released when the fibrous structure of the cytoplasmic skeleton is disrupted. In the nucleus, the LINC complex is directly coupled with lamin A at the INM and is involved in maintaining the structure of lamin A [56]. Knockdown of lamin A relocates nesprin-2 in the endoplasmic reticulum and leads to more mobile SUN1 and SUN2 proteins [56,57]. When mechanical force is applied to the nesprin protein, nuclear stiffness is increased, and lamin A is enriched in the LINC complex [58], which may cause its structure to be more compact. It has also been reported that increased external tension can induce soluble lamin A to assemble into the fibrous lamina [59,60]. These studies suggest that there are mechanical force-based connections between the LINC complex and the lamin A network. External stressful mechanical forces may contribute to assembly of lamin A proteins through the LINC complex. Collectively, we suggest that disruption of cytoplasmic skeleton fibers by blebbistatin or nocodazole may reduce the tension of the LINC complex, which may allow for a more relaxed lamin A submicroscopic network structure.

Another possible mechanism for the effect of cytoplasmic skeleton disruption on the lamin A network is phosphorylation modifications. Phosphorylation of lamin A at Ser 22 promotes disassembly of lamin A proteins from the network structure [61]. The content of lamin A phosphorylation regulates the stability of the lamin A network structure and interaction between lamin A and the LINC complex [57,62,63]. Although the specific pathways regulating lamin A phosphorylation are uncertain, it has been shown that increased cellular tension decreases the intracellular phosphorylated lamin A content [62]. Similarly, we found an increase in phosphorylated lamin A proteins after disruption of the cytoplasmic skeleton, which may be partly responsible for the loosening of the lamin A submicroscopic network. In general, the cytoplasmic skeleton may affect the submicroscopic structure of lamin A through LINC complexes, lamin A phosphorylation or other pathways. However, the complete molecular mechanism of this process is still unclear and needs to be investigated further.

The mechanical properties of the nucleus are mainly maintained by the lamin A protein [6,41]. It has been shown that the absence of lamin A severely reduces the stiffness of the nucleus [7,40,41]. Intriguingly, our study found that disruption of cytoplasmic skeletons did not reduce lamin A protein expression but did result in decreases stiffness of the nucleus, which seems to contradict previous research. The reason may be that destruction of the cytoplasmic skeleton reduces the density of the lamin A network. This suggests that the fibrous lamin A network structure strongly contributes to maintaining the stiffness of the nucleus.

The role of lamin in regulating gene transcription and chromatin spatial structure is indisputable [6,60]. Complexes of lamin A and lamin B receptor (LBR) are anchored on LADs and enrich heterochromatin to the nuclear membrane [64,65]. We found that disruption of the cytoplasmic skeletal fibril structure resulted in a change in the spatial distribution and relative volume of chromosomes 2 and 18, which is similar to other results [66]. The reason for this may be that a loose lamin A network causes a decrease in the anchoring level of heterochromatin on the nuclear membrane, which affects the overall spatial distribution of chromosomes.

Here, we demonstrate that the cytoplasmic skeletal fibril structure can affect the 3D morphology of the nucleus, the stiffness of the nucleus and the spatial distribution of chromosomes. For the first time, we found that disruption of the cytoplasmic skeleton reduces the denseness of the lamin A submicroscopic network, contributing to understanding the regulatory mechanisms of mechanical signals in the nucleus and the signaling pathways of cell mechanics. We also developed a new image quantization algorithm to quantify the characteristics of the whole lamin A submicroscopic network in 3D. The algorithm shows the influence of the cytoplasmic skeleton on the details of the lamin A 3D network, and this algorithm may be useful for analyzing the structural features of the lamin submicroscopic network in various physiological or pathological cells. Currently, there are numerous unanswered questions about the mechanisms regulating the overall mechanical structure of the cytoskeleton. Our study contributes to resolving the effect of the cytoplasmic skeleton on the 3D submicroscopic structure of the lamin A network and promoting elucidation of the trans-nuclear membrane regulation mechanism of cytoplasmic skeleton and lamin A network.

3.1. Limitations of the study

In the present study, we developed a quantitative analysis method for the lamin A 3D structure based on SIM imaging. However, this approach still faces several challenges. SIM allows for the super-resolution imaging of lamin A without the need for complex hardware and simple staining methods, which is unachievable with conventional optical microscopy, thus accelerating the pace of scientific research. Due the 120 nm optical diffraction limit of SIM, ordinary SIM cannot resolve lamin A networks below this limit. Combining sample preparation with Expansion Microscopy (ExM) technology could enable the quantitative analysis of higher-resolution lamin A 3D networks in conjunction with our quantitative imaging algorithm.

4. STAR methods

4.1. Cell culture and reagent treatment

The U2OS cell line (Meisen, CTCC-001-004) was used in this study. The cells were cultured in McCoy's 5A medium (Gibco) supplemented with 10 % fetal bovine serum (Gibco) and 1 % antibiotic/antimycotic solution (Gibco) in a humidified 5 % CO2 atmosphere at 37 °C. Before experiments, U2OS cells were incubated in medium with 25 μM blebbistatin (Sigma–Aldrich) or 2 μM nocodazole (Sigma–Aldrich) diluted with DMSO for 8 h after adhering for 24 h, with ~80 % coverage. The treated cells were then used for imaging, western blotting or AFM experiments.

4.2. Immunocytochemistry

U2OS cells were seeded in glass bottom dishes, fixed with 4 % paraformaldehyde for 15 min, permeabilized with 0.2 % Triton-X100 diluted with PBS for 15 min and blocked with 4 % bovine serum albumin diluted with 0.1 % Triton-X100 for 2 h. F-actin, tubulin, lamin A or phospho-lamin A in the fixed cells were stained with phalloidin or primary antibodies (phalloidin-Alexa Fluor 647 (Invitrogen, A22287), mouse anti alpha-tubulin (Abcam, Cat# ab7291), rabbit anti lamin A (Abcam, Cat# ab26300) (only labeled lamin A), or rabbit anti phospho-lamin A (Cell Signaling, 13448T), dilution 1:200) in blocking buffer for 14–16 h at 4 °C and then washed three times with PBS for 20 min. Secondary antibodies (donkey anti rabbit IgG-Alexa Fluor 488 (Abcam, Cat# ab150073) and goat anti mouse IgG-Alexa Fluor 555 (Abcam, Cat# ab150118), dilution 1:200) in PBS were incubated with the cells for 2 h at room temperature, and the cells were washed three times with PBS for 20 min. The labeled cells were stained with DAPI (Abcam, Cat# ab228549) for 15 min, washed three times with PBS for 5 min and stored at 4 °C or imaged immediately.

4.3. Microscopy imaging

Confocal imaging of cells was performed using a Leica SP5 laser scanning confocal microscope equipped with a 100 × /1.45 NA Plan Apo oil-immersion objective and four laser beams (405 nm, 488 nm, 561 nm and 642 nm). For Lattice SIM imaging, a Zeiss Elyra 7 super-resolution imaging microscope equipped with a 63 × /1.40 NA Plan-Apochromat objective or 10 × /0.3 NA EC Plan-Neofluar objective and four laser beams (405 nm, 488 nm, 561 nm and 647 nm) were used. For confocal imaging, 405 nm, 561 nm and 642 nm lasers were used to excite DAPI (nucleus), Alexa Fluor 555 (tubulin) and Alexa Fluor 647 (F-actin). For Lattice SIM imaging, 405 nm, 488 nm and 561 nm lasers were used to excite DAPI (nucleus), Alexa Fluor 488 or XCP 2 green (lamin A, phosphor-lamin A or chromosome 2) and XCP 18 orange (chromosome 18). Z-stack images of Lattice SIM were captured with a step size of 0.1 μm and enough steps to cover an intact nucleus for lamin A and chromosome imaging. To analyze the mean fluorescence intensity of phosphor-lamin A, "Tile Scan" and "Z-stack" mode in Elyra 7 were used to capture the fluorescence signal of each intact nucleus with the 10 × /0.3 NA EC Plan-Neofluar objective, and all Z-stack images were merged into one image by maximum intensity projection.

4.4. Image quantization algorithm for the lamin A submicroscopic network

All lamin A network reconfiguration and quantitative analysis were performed using Arivis software (Zeiss Arivis Pro). First, a mask was made on the lamin A 3D network fluorescence image, and the target analysis area was generated. Morphological closing preprocessing was performed on the target area such that the structure with uneven network connections formed a closed loop. Then we used the intelligent segmentation tool Blob Finder, which is based on the threshold detection and target structure detection algorithm in Arivis Pro, to segment the preprocessed image so as to obtain the preliminary network object. To make the segmented object form a complete network structure, we used object merging and the filter function to filter out nontarget signals to obtain a complete 3D network structure object.

To reconstruct the lamin A 3D network skeleton structure, we created a customized skeleton analysis script based on Arivis Pro. This code includes scripting commands using the Python digital image processing package with the Arivis image core (a powerful library dedicated to big data image processing). Notably, the parameters set in this script are suitable for tubular structure datasets with single block analysis. The parameters should be correspondingly modified when used to analyze other datasets.

After obtaining a complete 3D network structure object according to the above process, we set the corresponding object tag in the script, which will indicate which object in the software should be analyzed and calculated. The first step in this script is to create a binary mask to identify the location of the lamin A 3D network (Fig. S2).

Lee's algorithm was integrated to extract the 3D skeleton structure of the lamin A 3D network in Arivis software [67]. Its function is to reduce each connected component in the binary image to a single-pixel wide skeleton (Fig. S3A). The method of Lee's algorithm uses an octree data structure to examine a 3 × 3 × 3 neighborhood of a pixel. The algorithm proceeds by iteratively sweeping over the image and removing pixels at each iteration until the image stops changing. Each iteration consists of two steps: first, a list of candidates for removal is assembled; then, pixels from this list are rechecked sequentially to better preserve the connectivity of the image.

When completing the 3D skeleton calculation [68], we can obtain information on the branch points (Fig. S3B); the branch points are defined as follows: the node belongs to the voxel point on the 3D network, and there are at least two edge length vectors in different directions around the point. The branch lengths are also calculated by the connection of adjacent branch points (Fig. S3B). Then, the tubular segmentation function was also employed to achieve high-quality 3D visualization of the branch lengths (Figs. S3C and S3D).

Finally, based on the extracted 3D network skeleton, the Membrane-based Segmenter segmentation tool in Arivis Pro software was

used to reconstruct the 3D mesh of the whole lamin A network. Based on all the above analysis steps, we finally calculated the geometric parameters of the lamin A submicroscopic network, such as the number of branch points and meshes, the side length of the meshes and the 3D volume of the meshes. The side length of the meshes is equal to the branch length of the corresponding meshes.

4.5. Western blotting

Cells in the DMSO group or treated with blebbistatin or nocodazole were lysed with RIPA buffer (0.1 % SDS, 1 % sodium deoxycholate, 1 % NP-40, 150 mM NaCl, 50 mM Tris–HCl, 1 mM EDTA, pH = 7.4). Total lysates were quantified in a SYNERGY-H1 (BioTek) using an Enhanced BCA Protein Assay Kit. Approximately 30 μg of protein was resolved by SDS–PAGE and transferred to nitrocellulose membranes. The membranes were blocked with 5 % nonfat milk and probed with primary antibodies (rabbit anti lamin A (Abcam), dilution 1:1000) at 4 °C overnight. After the membranes were incubated with HRP-linked secondary antibodies (Goat Anti-Rabbit IgG (Abcam), dilution 1:2000), the blots were visualized with ChemiScope (CLINX Science Instruments). GAPDH protein was used as the loading control.

4.5.1. Extraction of nuclei

U2OS cells, plated at 80 % confluency in 60 mm culture dishes, were trypsinized in 0.25 % trypsin/EDTA (Gibco) and harvested by centrifugation at 200×*g* for 3 min. The cells were resuspended in 1 × PBS and numbered ~1,000,000 individuals for the next experiment by blood cell counting plate. The cells were centrifuged in a conical centrifuge tube at 600×*g* for 3 min, and then remove the supernatant. One milliliter of nuclear extraction (NE) buffer (20 μl 1 M HEPES-KOH pH = 7.9, 10 μl 1 M KCl, 0.25 μl 2 M spermidine, 10 μl 10 % Triton X-100, 200 μl glycerol, 760 μl ddH2O and 20 μl 50 × Complete Protease Inhibitor buffer (1 Roche Complete Protease Inhibitor EDTA-Free in 1 × PBS)) was used to resuspend the U2OS cells. The cells in NE buffer were incubated in ice for 10 min and centrifuged for 4 min at 1300×*g* at 4 °C. The nuclei in the sediment were resuspended in 1 ml 1 × PBS and centrifuged for 4 min at 1200×*g* at 4 °C. Then, the supernatant was removed, and the sediment was resuspended in 1 × PBS. After resuspension, the solution was transferred to poly-D-lysine-coated glass bottom dishes for 30 min, and 1 × PBS was used to remove unattached nuclei.

4.5.2. Stiffness measurement and analysis by atomic force microscopy

The stiffness measurement of the nucleus was achieved using a NanoWizard4XP AFM (Bruker), and a Scan Asyst-Fluid cantilever, as modified with a 9 μm polystyrene bead. The cantilever defection sensitivity was calibrated using an uncoated Petri dish. In indentation experiments, the extracted nucleus was probed 5 times at the center position by a cantilever. Deformation of the nucleus was determined by deducting the deflection of the cantilever in the force curves, and the nuclear stiffness was obtained by dividing the force amplitude of the nucleus by the deformation of the nucleus. All the AFM data were processed by JPKSPM Data Processing software.

4.5.3. Chromosome painting

U2OS cells were seeded on round coverslips with a 22 mm diameter. The cells were fixed with 3:1 methanol/acetic acid at −20 °C for 20 min at cell coverage of ~70 %. The cells were treated with 5 μl of chromosome 2 and 18 painting probe (Metasystems, D-0302-100-FI XCP 2 and D-0318-100-OR XCP 18, DE), covered by a glass slide and sealed by rubber cement. The sample with the probe was denatured on a hotplate at 75 °C for 2 min and then incubated at 37 °C overnight in a humidified box. After removing the coverslips from the glass slide, the sample was washed in 0.4 × SSC (pH = 7.0) at 72 °C for 2 min. Subsequently, the sample was washed in 2 × SSC with 0.05 % Tween-20 (pH = 7.0) at room temperature for 30 s and rinsed in PBS for 30 s. The labeled cells were finally mounted on glass slides with DAPI and imaged by Lattice SIM.

4.6. Statistical analysis

All confocal image processing was performed using Leica LAS X software, and the Lattice SIM image was processed by ZEN blue and ZEN black software.

Student's *t*-test was performed in Prism. Using ImageJ, the mean fluorescence intensity of phosphorylated lamin A and the normalized gray value of lamin A in western blots were measured.

The rendering graphs of the chromosomes and nuclei were performed in the "Surface" function of IMARIS. The volume and center position of the chromosomes and nuclei were exported directly. Considering the influence of differences in cell cycle and karyotype on chromosome copy number, only nuclei with the same chromosome copy were selected for chromosome painting analysis [44,69]. The relative distance of each copy of chromosomes from the nucleus center is calculated according to the spatial coordinates of chromosomes and nucleus. In order to exclude the effect of chromosome size on the position of chromosomes relative to the nucleus center, the weighted distance of a single copy of chromosome from the nucleus center was calculated using the ratio of the volume of each chromosome copy to the total volume of chromosomes in a single nucleus. The sum of the weighted distances of all chromosome copies in the nucleus is normalized by the cube root of the nucleus volume to obtain the relative position of chromosomes to the nucleus center.

Data availability statement

The original contributions presented in this study are included in the article and its supplementary materials. No data were

deposited in any publicly available repositories.

Funding and acknowledgements

This work was supported by the Natural Science Foundation of Yunnan Province (grant numbers 202001BC070001 and 202102AA100053), Shenzhen Bay Laboratory Open Program (grant numbers SZBL2021080601012) and Shenzhen Bay Laboratory - Evident Company Cooperation Fund.

CRediT authorship contribution statement

Zhenyu Yang: Writing – original draft, Visualization, Resources, Methodology, Investigation, Formal analysis, Data curation, Conceptualization. **Xianglong Liu:** Writing – original draft, Visualization, Validation, Formal analysis, Data curation. **Xiaoliang Li:** Visualization, Software, Resources, Data curation. **Maurizio Abbate:** Software, Resources, Data curation. **Han Rui:** Writing – review & editing, Investigation, Formal analysis. **Miao Guan:** Supervision, Project administration, Funding acquisition. **Zhenglong Sun:** Writing – review & editing, Supervision, Project administration, Methodology, Investigation, Funding acquisition, Conceptualization.

Declaration of competing interest

The authors declare that they have no known competing financial interests or personal relationships that could have appeared to influence the work reported in this paper.

Appendix A. Supplementary data

Supplementary data to this article can be found online at https://doi.org/10.1016/j.heliyon.2024.e36583.

References

[1] T.D. Pollard, R.D. Goldman, Overview of the cytoskeleton from an evolutionary perspective, Cold Spring Harbor Perspect. Biol. 10 (7) (2018), https://doi.org/10.1101/cshperspect.a030288.
[2] S. SenGupta, C.A. Parent, J.E. Bear, The principles of directed cell migration, Nat. Rev. Mol. Cell Biol. 22 (8) (2021) 529–547, https://doi.org/10.1038/s41580-021-00366-6.
[3] K.M. Grimes, V. Prasad, J.W. McNamara, Supporting the heart: functions of the cardiomyocyte's non-sarcomeric cytoskeleton, J. Mol. Cell. Cardiol. 131 (2019) 187–196, https://doi.org/10.1016/j.yjmcc.2019.04.002.
[4] J. Ahn, I. Jo, S.M. Kang, S. Hong, S. Kim, S. Jeong, Y.H. Kim, B.J. Park, N.C. Ha, Structural basis for lamin assembly at the molecular level, Nat. Commun. 10 (1) (2019) 3757, https://doi.org/10.1038/s41467-019-11684-x.
[5] D.E. Jaalouk, J. Lammerding, Mechanotransduction gone awry, Nat. Rev. Mol. Cell Biol. 10 (1) (2009) 63–73, https://doi.org/10.1038/nrm2597.
[6] N.L. Ovsiannikova, S.V. Lavrushkina, A.V. Ivanova, L.M. Mazina, O.A. Zhironkina, I.I. Kireev, Lamin A as a determinant of mechanical properties of the cell nucleus in health and disease, Biochemistry (Mosc). 86 (10) (2021) 1288–1300, https://doi.org/10.1134/S0006297921100102.
[7] J. Lammerding, L.G. Fong, J.Y. Ji, K. Reue, C.L. Stewart, S.G. Young, R.T. Lee, Lamins A and C but not lamin B1 regulate nuclear mechanics, J. Biol. Chem. 281 (35) (2006) 25768–25780, https://doi.org/10.1074/jbc.M513511200.
[8] M.J. Stroud, I. Banerjee, J. Veevers, J. Chen, Linker of nucleoskeleton and cytoskeleton complex proteins in cardiac structure, function, and disease, Circ. Res. 114 (3) (2014) 538–548, https://doi.org/10.1161/CIRCRESAHA.114.301236.
[9] F. Haque, D.J. Lloyd, D.T. Smallwood, C.L. Dent, C.M. Shanahan, A.M. Fry, R.C. Trembath, S. Shackleton, SUN1 interacts with nuclear lamin A and cytoplasmic nesprins to provide a physical connection between the nuclear lamina and the cytoskeleton, Mol. Cell Biol. 26 (10) (2006) 3738–3751, https://doi.org/10.1128/mcb.26.10.3738-3751.2006.
[10] M. Hieda, T. Matsumoto, M. Isobe, S. Kurono, K. Yuka, S. Kametaka, J.Y. Wang, Y.H. Chi, K. Kameda, H. Kimura, N. Matsuura, S. Matsuura, The SUN2-nesprin-2 LINC complex and KIF20A function in the Golgi dispersal, Sci. Rep. 11 (1) (2021) 5358, https://doi.org/10.1038/s41598-021-84750-4.
[11] P. Gimpel, Y.L. Lee, R.M. Sobota, A. Calvi, V. Koullourou, R. Patel, K. Mamchaoui, F. Nedelec, S. Shackleton, J. Schmoranzer, B. Burke, B. Cadot, E.R. Gomes, Nesprin-1alpha-Dependent microtubule nucleation from the nuclear envelope via Akap450 is necessary for nuclear positioning in muscle cells, Curr. Biol. 27 (19) (2017) 2999–3009 e9, https://doi.org/10.1016/j.cub.2017.08.031.
[12] D.J. Procter, C. Furey, A.G. Garza-Gongora, S.T. Kosak, D. Walsh, Cytoplasmic control of intranuclear polarity by human cytomegalovirus, Nature 587 (7832) (2020) 109–114, https://doi.org/10.1038/s41586-020-2714-x.
[13] T. Thomas, Cytoskeleton organizes nucleus, Nat. Struct. Mol. Biol. 29 (11) (2022) 1037, https://doi.org/10.1038/s41594-022-00870-z.
[14] D.A. Fletcher, R.D. Mullins, Cell mechanics and the cytoskeleton, Nature 463 (7280) (2010) 485–492, https://doi.org/10.1038/nature08908.
[15] J. Zonderland, I.L. Moldero, S. Anand, C. Mota, L. Moroni, Dimensionality changes actin network through lamin A/C and zyxin, Biomaterials 240 (2020) 119854, https://doi.org/10.1016/j.biomaterials.2020.119854.
[16] J.K. Kim, A. Louhghalam, G. Lee, B.W. Schafer, D. Wirtz, D.H. Kim, Nuclear lamin A/C harnesses the perinuclear apical actin cables to protect nuclear morphology, Nat. Commun. 8 (1) (2017) 2123, https://doi.org/10.1038/s41467-017-02217-5.
[17] J.R. Fan, L.R. You, W.J. Wang, W.S. Huang, C.T. Chu, Y.H. Chi, H.C. Chen, Lamin A-mediated nuclear lamina integrity is required for proper ciliogenesis, EMBO Rep. 21 (10) (2020) e49680, https://doi.org/10.15252/embr.201949680.
[18] D. Borin, B. Pena, S.N. Chen, C.S. Long, M.R.G. Taylor, L. Mestroni, O. Sbaizero, Altered microtubule structure, hemichannel localization and beating activity in cardiomyocytes expressing pathologic nuclear lamin A/C, Heliyon 6 (1) (2020) e03175, https://doi.org/10.1016/j.heliyon.2020.e03175.
[19] M. Stiekema, F.C.S. Ramaekers, D. Kapsokalyvas, M. van Zandvoort, R.J.A. Veltrop, J.L.V. Broers, Super-resolution imaging of the A- and B-type lamin networks: a comparative study of different fluorescence labeling procedures, Int. J. Mol. Sci. 22 (19) (2021), https://doi.org/10.3390/ijms221910194.
[20] A.F.L. Schneider, L.S. Benz, M. Lehmann, C.P.R. Hackenberger, Cell-permeable nanobodies allow Dual-Color super-resolution microscopy in untransfected living cells, Angew Chem. Int. Ed. Engl. 60 (40) (2021) 22075–22080, https://doi.org/10.1002/anie.202103068.
[21] W. Xie, A. Chojnowski, T. Boudier, J.S. Lim, S. Ahmed, Z. Ser, C. Stewart, B. Burke, A-Type lamins form distinct filamentous networks with differential nuclear pore complex associations, Curr. Biol. 26 (19) (2016) 2651–2658, https://doi.org/10.1016/j.cub.2016.07.049.

[22] M. Kittisopikul, L. Virtanen, P. Taimen, R.D. Goldman, Quantitative analysis of nuclear lamins imaged by super-resolution light microscopy, Cells 8 (4) (2019), https://doi.org/10.3390/cells8040361.

[23] A.M. Rozario, A. Morey, C. Elliott, B. Russ, D.R. Whelan, S.J. Turner, T.D.M. Bell, 3D single molecule super-resolution microscopy of whole nuclear lamina, Front. Chem. 10 (2022) 863610, https://doi.org/10.3389/fchem.2022.863610.

[24] M. Kovacs, J. Toth, C. Hetenyi, A. Malnasi-Csizmadia, J.R. Sellers, Mechanism of blebbistatin inhibition of myosin II, J. Biol. Chem. 279 (34) (2004) 35557–35563, https://doi.org/10.1074/jbc.M405319200.

[25] A.F. Straight, A. Cheung, J. Limouze, I. Chen, N.J. Westwood, J.R. Sellers, T.J. Mitchison, Dissecting temporal and spatial control of cytokinesis with a myosin II Inhibitor, Science 299 (5613) (2003) 1743–1747, https://doi.org/10.1126/science.1081412.

[26] S. Florian, T.J. Mitchison, Anti-microtubule drugs, Methods Mol. Biol. 1413 (2016) 403–421, https://doi.org/10.1007/978-1-4939-3542-0_25.

[27] A. Rauscher, M. Gyimesi, M. Kovács, A. Málnási-Csizmadia, Targeting myosin by blebbistatin derivatives: optimization and pharmacological potential, Trends Biochem. Sci. 43 (9) (2018) 700–713, https://doi.org/10.1016/j.tibs.2018.06.006.

[28] K. Atluri, A.M. De Jesus, S. Chinnathambi, M.J. Brouillette, J.A. Martin, A.K. Salem, E.A. Sander, Blebbistatin-loaded poly(d,l-lactide-co-glycolide) particles for treating Arthrofibrosis, ACS Biomater. Sci. Eng. 2 (7) (2016) 1097–1107, https://doi.org/10.1021/acsbiomaterials.6b00082.

[29] J.C. Molero, J.P. Whitehead, T. Meerloo, D.E. James, Nocodazole inhibits insulin-stimulated glucose transport in 3T3-L1 adipocytes via a microtubule-independent mechanism, J. Biol. Chem. 276 (47) (2001) 43829–43835, https://doi.org/10.1074/jbc.M105452200.

[30] P. Chen, D.Q. Xu, S.L. Xu, H. Xiao, S.H. Wan, X.H. Wang, M.E. DiSanto, X.H. Zhang, Blebbistatin modulates prostatic cell growth and contrapctility through myosin II signaling, Clin Sci (Lond). 132 (20) (2018) 2189–2205, https://doi.org/10.1042/cs20180294.

[31] K. Nagano, T. Shinkawa, H. Mutoh, O. Kondoh, S. Morimoto, N. Inomata, M. Ashihara, N. Ishii, Y. Aoki, M. Haramura, Phosphoproteomic analysis of distinct tumor cell lines in response to nocodazole treatment, Proteomics 9 (10) (2009) 2861–2874, https://doi.org/10.1002/pmic.200800667.

[32] Z. Liu, L.A. van Grunsven, E. Van Rossen, B. Schroyen, J.P. Timmermans, A. Geerts, H. Reynaert, Blebbistatin inhibits contraction and accelerates migration in mouse hepatic stellate cells, Br. J. Pharmacol. 159 (2) (2010) 304–315, https://doi.org/10.1111/j.1476-5381.2009.00477.x.

[33] M.E. Grady, R.J. Composto, D.M. Eckmann, Cell elasticity with altered cytoskeletal architectures across multiple cell types, J. Mech. Behav. Biomed. Mater. 61 (2016) 197–207, https://doi.org/10.1016/j.jmbbm.2016.01.022.

[34] P. Bhattacharjee, D. Dasgupta, K. Sengupta, Molecular events in lamin B1 Homopolymerization: a Biophysical characterization, J. Phys. Chem. B 119 (44) (2015) 14014–14021, https://doi.org/10.1021/acs.jpcb.5b07320.

[35] S. Mishra, D.L. Levy, Nuclear F-actin and Lamin A antagonistically modulate nuclear shape, J. Cell Sci. 135 (13) (2022), https://doi.org/10.1242/jcs.259692.

[36] Z. Tariq, H. Zhang, A. Chia-Liu, Y. Shen, Y. Gete, Z.M. Xiong, C. Tocheny, L. Campanello, D. Wu, W. Losert, K. Cao, Lamin A and microtubules collaborate to maintain nuclear morphology, Nucleus 8 (4) (2017) 433–446, https://doi.org/10.1080/19491034.2017.1320460.

[37] M. Stiekema, F. Houben, F. Verheyen, M. Borgers, J. Menzel, M. Meschkat, M. van Zandvoort, F.C.S. Ramaekers, J.L.V. Broers, The role of lamins in the nucleoplasmic reticulum, a Pleiomorphic organelle that enhances Nucleo-cytoplasmic interplay, Front. Cell Dev. Biol. 10 (2022) 914286, https://doi.org/10.3389/fcell.2022.914286.

[38] B.D. Cosgrove, C. Loebel, T.P. Driscoll, T.K. Tsinman, E.N. Dai, S.J. Heo, N.A. Dyment, J.A. Burdick, R.L. Mauck, Nuclear envelope wrinkling predicts mesenchymal progenitor cell mechano-response in 2D and 3D microenvironments, Biomaterials 270 (2021) 120662, https://doi.org/10.1016/j.biomaterials.2021.120662.

[39] K.V. Iyer, A. Taubenberger, S.A. Zeidan, N.A. Dye, S. Eaton, F. Jülicher, Apico-basal cell compression regulates Lamin A/C levels in epithelial tissues, Nat. Commun. 12 (1) (2021) 1756, https://doi.org/10.1038/s41467-021-22010-9.

[40] M. Goelzer, A. Dudakovic, M. Olcum, B. Sen, E. Ozcivici, J. Rubin, A.J. van Wijnen, G. Uzer, Lamin A/C is dispensable to mechanical repression of Adipogenesis, Int. J. Mol. Sci. 22 (12) (2021), https://doi.org/10.3390/ijms22126580.

[41] L.K. Srivastava, Z. Ju, A. Ghagre, A.J. Ehrlicher, Spatial distribution of lamin A/C determines nuclear stiffness and stress-mediated deformation, J. Cell Sci. 134 (10) (2021), https://doi.org/10.1242/jcs.248559.

[42] B. Burke, C.L. Stewart, The nuclear lamins: flexibility in function, Nat. Rev. Mol. Cell Biol. 14 (1) (2013) 13–24, https://doi.org/10.1038/nrm3488.

[43] E. Lund, A.R. Oldenburg, E. Delbarre, C.T. Freberg, I. Duband-Goulet, R. Eskeland, B. Buendia, P. Collas, Lamin A/C-promoter interactions specify chromatin state-dependent transcription outcomes, Genome Res. 23 (10) (2013) 1580–1589, https://doi.org/10.1101/gr.159400.113.

[44] L. Chang, M. Li, S. Shao, C. Li, S. Ai, B. Xue, Y. Hou, Y. Zhang, R. Li, X. Fan, A. He, C. Li, Y. Sun, Nuclear peripheral chromatin-lamin B1 interaction is required for global integrity of chromatin architecture and dynamics in human cells, Protein Cell 13 (4) (2022) 258–280, https://doi.org/10.1007/s13238-020-00794-8.

[45] P.K. Geyer, M.W. Vitalini, L.L. Wallrath, Nuclear organization: taking a position on gene expression, Curr. Opin. Cell Biol. 23 (3) (2011) 354–359, https://doi.org/10.1016/j.ceb.2011.03.002.

[46] B. Burke, LINC complexes as regulators of meiosis, Curr. Opin. Cell Biol. 52 (2018) 22–29, https://doi.org/10.1016/j.ceb.2018.01.005.

[47] M. Kittisopikul, T. Shimi, M. Tatli, J.R. Tran, Y. Zheng, O. Medalia, K. Jaqaman, S.A. Adam, R.D. Goldman, Computational analyses reveal spatial relationships between nuclear pore complexes and specific lamins, J. Cell Biol. 220 (4) (2021), https://doi.org/10.1083/jcb.202007082.

[48] A. Kumar, G.V. Shivashankar, Dynamic interaction between actin and nesprin2 maintain the cell nucleus in a prestressed state, Methods Appl. Fluoresc. 4 (4) (2016) 044008, https://doi.org/10.1088/2050-6120/4/4/044008.

[49] L. Wang, S.C. Paudyal, Y. Kang, M. Owa, F.X. Liang, A. Spektor, H. Knaut, I. Sanchez, B.D. Dynlacht, Regulators of tubulin polyglutamylation control nuclear shape and cilium disassembly by balancing microtubule and actin assembly, Cell Res. 32 (2) (2022) 190–209, https://doi.org/10.1038/s41422-021-00584-9.

[50] A.D. Stephens, E.J. Banigan, J.F. Marko, Chromatin's physical properties shape the nucleus and its functions, Curr. Opin. Cell Biol. 58 (2019) 76–84, https://doi.org/10.1016/j.ceb.2019.02.006.

[51] G. Gerlitz, O. Reiner, M. Bustin, Microtubule dynamics alter the interphase nucleus, Cell. Mol. Life Sci. 70 (7) (2013) 1255–1268, https://doi.org/10.1007/s00018-012-1200-5.

[52] R.M. Stewart, A.E. Zubek, K.A. Rosowski, S.M. Schreiner, V. Horsley, M.C. King, Nuclear-cytoskeletal linkages facilitate cross talk between the nucleus and intercellular adhesions, J. Cell Biol. 209 (3) (2015) 403–418, https://doi.org/10.1083/jcb.201502024.

[53] X. Zhang, K. Lei, X. Yuan, X. Wu, Y. Zhuang, T. Xu, R. Xu, M. Han, SUN1/2 and Syne/Nesprin-1/2 complexes connect centrosome to the nucleus during neurogenesis and neuronal migration in mice, Neuron 64 (2) (2009) 173–187, https://doi.org/10.1016/j.neuron.2009.08.018.

[54] E. Carley, R.M. Stewart, A. Zieman, I. Jalilian, D.E. King, A. Zubek, S. Lin, V. Horsley, M.C. King, The LINC complex transmits integrin-dependent tension to the nuclear lamina and represses epidermal differentiation, Elife 10 (2021), https://doi.org/10.7554/eLife.58541.

[55] E. Carley, M.C. King, S. Guo, Integrating mechanical signals into cellular identity, Trends Cell Biol. 32 (8) (2022) 669–680, https://doi.org/10.1016/j.tcb.2022.02.006.

[56] M. Crisp, Q. Liu, K. Roux, J.B. Rattner, C. Shanahan, B. Burke, P.D. Stahl, D. Hodzic, Coupling of the nucleus and cytoplasm: role of the LINC complex, J. Cell Biol. 172 (1) (2006) 41–53, https://doi.org/10.1083/jcb.200509124.

[57] M. Hieda, Implications for diverse functions of the LINC complexes based on the structure, Cells 6 (1) (2017), https://doi.org/10.3390/cells6010003.

[58] C. Guilluy, L.D. Osborne, L. Van Landeghem, L. Sharek, R. Superfine, R. Garcia-Mata, K. Burridge, Isolated nuclei adapt to force and reveal a mechanotransduction pathway in the nucleus, Nat. Cell Biol. 16 (4) (2014) 376–381, https://doi.org/10.1038/ncb2927.

[59] J. Swift, I.L. Ivanovska, A. Buxboim, T. Harada, P.C. Dingal, J. Pinter, J.D. Pajerowski, K.R. Spinler, J.W. Shin, M. Tewari, F. Rehfeldt, D.W. Speicher, D. E. Discher, Nuclear lamin-A scales with tissue stiffness and enhances matrix-directed differentiation, Science 341 (6149) (2013) 1240104, https://doi.org/10.1126/science.1240104.

[60] S. Osmanagic-Myers, T. Dechat, R. Foisner, Lamins at the crossroads of mechanosignaling, Gene Dev. 29 (3) (2015) 225–237, https://doi.org/10.1101/gad.255968.114.

[61] V. Kochin, T. Shimi, E. Torvaldson, S.A. Adam, A. Goldman, C.G. Pack, J. Melo-Cardenas, S.Y. Imanishi, R.D. Goldman, J.E. Eriksson, Interphase phosphorylation of lamin A, J. Cell Sci. 127 (Pt 12) (2014) 2683–2696, https://doi.org/10.1242/jcs.141820.

[62] A. Buxboim, J. Swift, J. Irianto, K.R. Spinler, P.C. Dingal, A. Athirasala, Y.R. Kao, S. Cho, T. Harada, J.W. Shin, D.E. Discher, Matrix elasticity regulates lamin-A, C phosphorylation and turnover with feedback to actomyosin, Curr. Biol. 24 (16) (2014) 1909–1917, https://doi.org/10.1016/j.cub.2014.07.001.
[63] A. Woglar, A. Daryabeigi, A. Adamo, C. Habacher, T. Machacek, A. La Volpe, V. Jantsch, Matefin/SUN-1 phosphorylation is part of a surveillance mechanism to coordinate chromosome synapsis and recombination with meiotic progression and chromosome movement, PLoS Genet. 9 (3) (2013) e1003335, https://doi.org/10.1371/journal.pgen.1003335.
[64] I. Solovei, A.S. Wang, K. Thanisch, C.S. Schmidt, S. Krebs, M. Zwerger, T.V. Cohen, D. Devys, R. Foisner, L. Peichl, H. Herrmann, H. Blum, D. Engelkamp, C. L. Stewart, H. Leonhardt, B. Joffe, LBR and lamin A/C sequentially tether peripheral heterochromatin and inversely regulate differentiation, Cell 152 (3) (2013) 584–598, https://doi.org/10.1016/j.cell.2013.01.009.
[65] M. Kohwi, J.R. Lupton, S.L. Lai, M.R. Miller, C.Q. Doe, Developmentally regulated subnuclear genome reorganization restricts neural progenitor competence in Drosophila, Cell 152 (1–2) (2013) 97–108, https://doi.org/10.1016/j.cell.2012.11.049.
[66] N.M. Ramdas, G.V. Shivashankar, Cytoskeletal control of nuclear morphology and chromatin organization, J. Mol. Biol. 427 (3) (2015) 695–706, https://doi.org/10.1016/j.jmb.2014.09.008.
[67] Chu Tclrlkcn, Building skeleton models via 3-D medial surface Axis thinning algorithms, Comput. Vis. Graph Image Process 56 (6) (1994) 462–478, https://doi.org/10.1006/cgip.1994.1042.
[68] T.Y. Zhang, C.Y. Suen, A fast parallel algorithm for thinning digital patterns, Commun. ACM 27 (3) (1984) 236–239, https://doi.org/10.1145/357994.358023.
[69] C. Raftopoulou, F.M. Roumelioti, E. Dragona, S. Gimelli, F. Sloan-Béna, V. Gorgoulis, S.E. Antonarakis, S. Gagos, Karyotypic flexibility of the complex cancer genome and the role of polyploidization in maintenance of structural integrity of cancer chromosomes, Cancers 12 (3) (2020), https://doi.org/10.3390/cancers12030591.